Highlights

- Spectroscopic Ellipsometry results showed plasmonic excitations with increased intensity as the average particle diameter increases.
- Scattering studies showed that the incorporation of Ag NPs enhances the non-specular reflectivity due to the scattering of light; the scattering is maximized and is not strongly affected by the angle of incidence.
- The resistivity of the hybrid layers is lower in relation to the single PEDOT:PSS sample.
- Under illumination the I-V characteristics of the plasmonic samples show slight deviations in the inclination of the curve, an indication that plasmonic excitations is a non-vanishing factor for their electrical performance.

Performance of hybrid buffer PEDOT:PSS layers doped with plasmonic silver nanoparticles

N. Kalfagiannis[1,2]*, P. G. Karagiannidis[1], C. Pitsalidis[1], N. Hastas[3], N. T. Panagiotopoulos[4], P. Patsalas[4], S. Logothetidis[1]

[1]Laboratory for Thin Films – Nanosystems and Nanometrology (LTFN), Physics Department, Aristotle University of Thessaloniki, GR-54124, Thessaloniki, Greece

[2]School of Science and Technology, Nottingham Trent University, NG11 8NS, Nottingham, United Kingdom

[3]Aristotle University of Thessaloniki, Physics Department, GR-54124, Thessaloniki, Greece

[4]University of Ioannina, Department of Materials Science and Engineering, GR-45110 Ioannina, Greece

Abstract

We compare the performance of a typical (for use as a hole transport layer in organic photovoltaics) PEDOT:PSS thin film [Poly(3,4-ethylenedioxythiophene) poly(styrenesulfonate)] with a series of PEDOT:PSS layers doped with silver nanoparticles (NPs) of various size distributions. These hybrid layers have attracted great attention as buffer layers in plasmonic organic photovoltaics (OPV), although there is no report up today on their isolated performance. In the present study we prepared a series of PEDOT:PSS layers sandwiched between ITO and Au electrodes. Ag NPs were deposited on top of the ITO by e-beam evaporation followed by the spin coating of PEDOT:PSS. Electrical characterization, under dark, showed linear resistive behavior for all the samples; lower resistance was observed for the hybrid ones. The resistivity decreases as the NPs size increases; preferential current paths formed in PEDOT:PSS through Ag NPs increase substantially the electric field between the ITO and the Au electrodes. A striking observation is the slight change in the inclination of the I-V curves when measured under illumination for the case of the plasmonic layers; an indication that changes in the electric field in the vicinity of the NP due to plasmonic excitation is a non-vanishing factor.

Keywords: surface plasmon resonance, enhanced scattering, hybrid buffer layers, PEDOT:PSS films, silver nanoparticles

1. Introduction

Organic Photovoltaics (OPVs) have attracted considerable attention because of their unique advantages of being light-weight, mechanically flexible, suitable for large scale production and potentially low cost alternative to their inorganic counterpart technology [1-4]. However, their efficiency and stability over lifetime improvement still remains a challenge for the practical applications of OPVs. Up to know the strategies for achieving higher efficiencies are scattered between various approaches, for example optimizing the morphology of the active layer and the charge transport properties of the absorber through thermal annealing treatment [5], the use of various types of organic solvents [6, 7], the use of additives [8] and the great variety of process conditions [6, 9, 10]. Recently though, much attention has been given to the introduction of metallic nanoparticles (NPs) in suitable places to trap or to forwards scatter light inside the active layer and enhance the absorption in the organic semiconductor film [11-30].

Lots of these reports found in literature deal with the incorporation of Ag or Au NPs in the PEDOT:PSS layer, serving as hole transport layer in OPVs. A. J. Morfa et al. have reported an increase in efficiency by a factor of 1.7 for bulk heterojunction solar cells when silver NPs are placed on top of the ITO film [12]. F. D. Dixon et al. have shown theoretical and experimental results supporting the very strong near field enhancement around Au NPs due to plasmonic excitations. However the electron density wave mainly distributes laterally along the PEDOT:PSS layer thus leading to minimal enhancement of light absorption into the photoactive layer [22]. Their results have been supported by Richard S. Kim et al. where they have reported on the EBE Ag NPs embedded in the PEDOT:PSS layer of an OPV device [29]. A significant increase in the power conversion efficiency of the plasmonic solar cell was experimentally observed through optical absorption enhancement close to the Localised Surface Plasmon Resonance (LSPR) in the case of cylindrical shaped NPs. Their results are supported by 3-Dimensional finite difference time domain (FDTD) where they also showed that excited LSPR modes from

spherical NPs is tightly localized in the vicinity of the NPs; thus such a configuration could hardly benefit the OPV device from enhanced absorption. More recently [30], it has been reported an extended study on the plasmonic effects in OPVs when size-controlled Ag NPs were incorporated into the anodic buffer layer. It has been reported an increase in the power conversion efficiency in various bulk heterojunction systems, used as active layers, upon embedding the Ag NPs. They also report on the enhanced absorption due to the plasmonic scattering effect, however they did not seem to have (at least for the particle concentration used in their study) any significant enhancement in the conductivity of the buffer layer when Ag NPs embedded , which comes in contradiction to other studies [22] and the findings of the present work.

Apart from the significant contribution to the device performance which is obvious from all the aforementioned published data it is still questionable how much the plasmonic excitations can affect the efficiency of the OPV and by what means. Thus, it is essential for the future design of plasmonic OPVs to focus on the effect of the isolated plasmonic layers (e.g. the hole transport layer or the active layer) and quantify their performance. In the present work, we present comparative results out of a standard PEDOT:PSS buffer layer - used as a hole transport layer (HTL) in OPVs - with a series of PEDOT:PSS layers doped with plasmonic Ag NPs of various size distributions.

2. Experimental

Ag NPs were deposited on top of pre-patterned ITO/glass substrates in the form of a discontinuous thin film by electron beam evaporation (EBE) within an ultra-high vacuum chamber (base pressure $<10^{-8}$ mbar). The target was operated at 6 V and 50 mA. A mass spectrometer monitored the gas phase during deposition while an ultra fast 32-wavelength spectroscopic ellipsometer (SE) was used to collect spectra every 250 ms. The spectra were analyzed real-time using a three-phase geometry model (air/Ag/ITO/Glass) and considering the Drude model [31] for Ag in order to monitor the thickness evolution of the thin film by recording the effective thickness data (the thickness of a Ag thin film considering it a simple smooth layer). Four distinct effective thicknesses (5, 10, 15, 20 nm) were chosen, leading to different particle size distributions. These films were then subjected to

thermal annealing (inside a glove-box) at 200 ^{o}C for 1min. Re-liquification and re-crystalization of Ag takes place in a few seconds; thus we can manipulate their shape and size going from shapeless grains to shperoidal ones.

Poly(3,4-ethylenedioxythiophene)/ Poly(styrenesulfonate) (PEDOT:PSS), with the commercial product name CLEVIOS P VP Al 4083, layer (60 ± 5 nm) was spun at 4000 rpm (on top of the annealed Ag samples) followed by annealing at 140 ^{o}C for 10 min, in order to remove the residual water. The device fabrication was finalized by the EBE of the cathode comprising from a 70 nm thin film of Au. The choice of Au as a cathode in our case lies on the fact of the ohmic contact between PEDOT:PSS and Au; thus easily we can extract the resistivity of the devices. Reference samples (without NPs) were prepared to detect alterations on the performance. Figure 1 shows the device architectures that were utilized in the present work: (a) for the reference device and (b-e) for the plasmonic ones. In the paragraphs to follow, we keep the same formalism (a-e) to designate individual layers (Ag/ITO) or bilayers (PEDOT:PSS/Ag/ITO) that have the same Ag particle distribution as the devices shown in Fig. 1.

The optical properties were investigated by Spectroscopic Ellipsometry (SE) from the Vis-fUV spectral region (1.5-6.5 eV) with a step of 20 meV, at an angle of incidence of 70°. The deposited Ag NPs and the PEDOT:PSS surface morphology were characterized by Atomic Force Microscopy. 2 x 2 μm^2 images were obtained and the distribution of the size of the particles was derived though grain analysis. For the light scattering study, a laser diode emitting polarized red light, with wavelength close to the observed LSPR in SE spectra (675.5 nm), and an in-house built apparatus consisting of a goniometer capable of independent movement between sample and detector (thus fulfilling the specular (θ-θ geometry) or non-specular (ω-tilt geometry) reflectance geometry) and a computer controlled analog photometer were used.

Finally, current – voltage (I–V) characteristics of the devices derived by a Keithley 2420 source measurement unit. The measurements were repeated under air mass (AM) 1.5G and 1000W/m^2 of illumination, to distinguish the performance of the individual layers under plasmonic excitation as well.

3. Results and discussion

3.1 Topography

Figure 2 depicts AFM images, captured in tapping mode, of Ag NPs, after thermal annealing (a-d). NPs comprise from spheroidal grains attached to the substrate. The surface statistical analysis indicated distributions varying from approximately 30 to 80 nm. This average size, as derived from grain analysis, resembles the diameter of a spherical particle with equivalent volume to the actual one. Cross sectional analysis at the same time indicates elongated particles in the X-Y dimension (Fig. 2f inset). EBE is capable of producing these kind of cylindrical NPs and as shown elsewhere [29] such particles can have an impact in the strong electric field enhancement arising from the corners of the cylinders that can be coupled to the photoactive absorption region [29, 33]. Results out of this analysis are summarized in Table 1.

The deposition of the PEDOT:PSS on top of the NPs seems to have no effect in the morphology of the sample with the smaller NPs (Fig. 3a). Indeed, a comparison of the AFM image of that sample and the reference one (Fig. 3e) shows no variation in the surface features concomitantly with similar RMS roughness values: 1.15 nm for the PEDOT:PSS sample and 1.18 nm for the PEDOT:PSS/Ag sample. As the particle size increases the RMS values are going as high as 3.24 nm and as it gets closer to the PEDOT:PSS thickness and further exceeds that there is a serious deviation from the standard topographic features of the buffer layer with spikes exceeding way up to the surface waviness of all the other samples (Fig. 3d). However, the cross sections snapshots (Fig. 3f) indicate that even the largest NPs must be covered by a thin PEDOT:PSS film. Comparing the two insets (Fig. 2f and Fig. 3f), that show a magnification of the cross section graph, one can recognize the different profiles of the particles itself and the profile of the particles covered by the PEDOT:PSS, especially in the X-axis where the buffer layer provides a X-Y area above 140 nm whereas the maximum size in the X-Y plane for the particles is up to 120 nm. Providing the necessary passivation to the NPs is of great importance not only for this study (to avoid direct contact between the particles and the cathode) but also for the consideration of an OPV device where the particles should be encapsulated to avoid direct contact with the photoactive layer. The later result is further proven by SE results that will follow in the next paragraph.

3.2 Spectroscopic Ellipsometry Results

Figure 4 shows the pseudo-dielectric function of the samples prior to the Au deposition. In the higher photon energies the contribution from the PEDOT:PSS interband transitions is apparent. In the lower photon energies the spectra is dominated by the LSPR modes of the hybrid samples. A slight redshift and an increase of the LSPR signal is apparent as the NPs increase in size. It has to be mentioned that this is an observation of the optical behavior of the samples which is not straightforward related to their electrical performance when incorporated in a full OPV device. However, the shape and the size of the particles in the present study (due to their cyclindrical shape), as discussed earlier [29,33] could possibly provide a benefit through the plasmonic excitations at the corners of the cylinders and promote the enhancement in absorption within the active layer.

The SE data were fitted using the Maxwell-Garnett effective medium approximation (MG-EMA) [32] considering a geometrical model consisting of Ag and PEDOT:PSS on top of an ITO/Glass substrate (air/PEDOT:PSS-Ag/ITO/Glass), taking into account the average size and shape of the NPs, as derived by the grain analysis. Thus, we assumed half elliptical particles (Fig. 5 inset) with $\alpha = \beta$ equal to the average particle diameter (X, Y plane) and γ equal to an average size, in Z axis, as derived by the cross sectional AFM analysis. The Ag optical constants were modeled using the Drude free-electron equation [31]:

$$\tilde{\varepsilon}(\omega) = \varepsilon_1(\omega) + i\varepsilon_2(\omega) = \varepsilon_\infty - \frac{\omega_p^2}{\omega^2 - i\Gamma\omega}, \quad (1)$$

where, ω_p is the bulk plasma frequency for Ag, Γ is the free electron relaxation frequency and ε_∞ is a constant above unity that is related to the contribution from interband transitions (that we do not take into account in the present analysis). A spectra of the sample with the largest NPs (real part-black squares and imaginary part-blue circles) and the fitting results (solid lines) are depicted in Fig. 5 in the visible spectral range, where the LSPR is apparent. From the fitting process it was possible to estimate that a thin 8 nm PEDOT:PSS film fully covers the particles. The dielectric function of ITO and its layer thickness were determined prior to the deposition of the Ag NPs.

3.3 Variable Angle Reflectance Measurements

The effect of incorporating plasmonic Ag NPs on the PEDOT:PSS layer can be evaluated by considering the light scattering data, presented in Fig. 6. The measured specular and off-specular reflectivity values were normalized to the specular reflectivity of a smooth Au film deposited on Si(100). For the case of this particular study we prepared samples of PEDOT:PSS/Ag/Glass to avoid any reflectance contribution from the ITO film. Figure 6 shows that the incorporation of Ag NPs enhances the non-specular reflectivity due to the scattering of light; the scattering is indeed maximized for the samples with the largest NPs distribution and it is not strongly affected to the angle of incidence. This is more clearly illustrated in the inset of Fig. 6 where the relative ratio of the total (specular + non-specular) reflectivity R over the specular reflectivity (R_s) values for the considered samples are recorded at a tilting angle of 20^o. It is evident that the contribution of the non-specular component is maximized for the samples with the largest NPs. Therefore, light scattering can contribute to the improvement of efficiency of a potential OPV device, through the excitation of electrons by photons to non-specular directions. However, the back scattering (reflectance) is also increasing with an increase in the size of the Ag NPs and is indeed maximized for the sample with the largest NPs. It has been shown [30] that the scattering to specular direction is growing stronger as the particle diameter exceeds the 75 nm which could be a drawback for the absorption enhancement on an OPV device. Although OPV devices could benefit out of the scattering to non-specular directions from large NPs there is still work to be done in the surface coverage manipulation of particles when these are deposited by a physical vapor deposition technique. A 55% of coverage for the largest NPs in the case of the present study might be enough to prevent light to efficiently penetrate the whole device structure.

3.4 Electrical characterization

Figure 7a shows the I-V curves of all the devices, reference (a) and plasmonic (b-e) ones. The resistivity decreases as the NP size increases (Fig. 7b). When a pure metal, like Ag NPs in the present work, is embedded into a p-type metal-like material, such as PEDOT:PSS, an increase in the recombination current may be expected due to higher recombination ratio between the free charge carriers of Ag NPs (electrons) and free charge carrier of PEDOT:PSS (holes). Thus, an increase to the total current flowing through the device may be expected, resulting to lower total resistance of the devices measured at dark. This result however should be independent to

the size of Ag NPs due to the fact that the embedded metal provides in any case the electrons which can be recombined with the PEDOT:PSS holes. Furthermore, the increase of the interface roughness between PEDOT:PSS and the metal electrodes usually increases the interface traps resulting in a reduction of free charge carriers and thus to a decrease of the total current flowing through the device. In the contrary, in our devices when Ag NPs height increases the surface roughness is increased and the resistance of the devices measured at dark is continuously decreasing showing (up to a certain point) that neither the recombination process nor the increase of the interface roughness are the dominating mechanisms. As a result, the only possible explanation is due to the fact that preferential current paths formed inside the hybrid layer through the particles, thus increasing substantially the electric field between the ITO bottom electrode and the Au top electrode. In conclusion, the voltage drop between the anode and the cathode becomes larger in the presence of the NPs providing a lower resistive path than the PEDOT:PSS itself. As the particle size increases the upper surface of PEDOT:PSS (on the Au electrode side) becomes substantially less providing the holes a shorter path towards the ITO electrode.

In addition to the measurements in the dark we performed measurements under illumination, to elucidate any difference in the electrical performance on the devices when plasmonic excitations are present. Indeed, only the hybrid devices showed a slight increase in the inclination of the I-V curves when captured under light. This is an indication that the enhancement of the electric field in the vicinity of the metal particles contributes to the behavior of the buffer layer. This can also be attributed to the thermal instability of the PEDOT:PSS layers. It has been shown [34] that a decrease of the resistivity in single PEDOT:PSS films is possible when samples are irradiated (under many successive cycles) and the difference between electrical resistivity in the dark and under irradiation becomes more important at higher temperatures. These observations indicate a combination of photon assisted and thermally activated mechanisms of conduction. While, in our case we do not report any difference in the pure PEDOT:PSS sample (the measurement lasts only a few seconds) the plasmonic particles may act as hot spots when the devices are irradiated, raising the temperature in their vicinity and thus producing variations in the inclination of the IV curve.

4. Conclusions

In the present work, we performed a comparative study on the performance of PEDOT:PSS individual layers doped with Ag NPs of various size distributions, sandwiched between ITO and Au electrodes. Their performance was compared with a single standard PEDOT:PSS layer. SE and Variable Angle Reflectance and Scattering measurements were used to quantify the plasmonic effect of the devices doped with the NPs in correlation with the device electrical characteristics, measured both in dark and under illumination. SE results showed enhanced absorption in the visible spectral for the plasmonic configurations and enhanced reflectance at 480 – 600 nm where the LSPR is apparent. At the same time scattering studies showed that the incorporation of Ag NPs enhances the non-specular reflectivity due to the scattering of light; the scattering is maximized and is not strongly affected by the angle of incidence, clearly illustrating that light scattering can contribute to the improvement of the device performance. Electrical measurements showed improved performance (lower resistivity) for the samples with the Ag NPs embedded in the PEDOT:PSS which could lead to lower series resistance values in an OPV device. The resistivity decreases further as the particle size increases reaching a plateau at around 60 nm of average particle diameter. When the same measurements were repeated under illumination a small but not vanishing effect on the inclination of the I-V curves for the plsamonic samples was observed indicating that plasmonic excitations can contribute to the electrical performance of the buffer layer and consequently to any potential OPV device.

References

[1] T.D. Nielsen, C. Cruickshank, S. Foged, J. Thorsen, F.C. Krebs, Solar Energy Materials and Solar Cells 94/10 (2010) 1553.

[2] N. Espinosa, R. Garcia-Valverde, A. Urbina, F.C. Krebs, Solar Energy Materials and Solar Cells 95/5 (2011) 1293.

[3] M. Jorgensen, K. Norrman, S.A. Gevorgyan, T. Tromholt, B. Andreasen, F.C. Krebs, Adv. Mater. 24/5 (2012) 580.

[4] R. Sondergaard, M. Hosel, D. Angmo, T.T. Larsen-Olsen, F.C. Krebs, Materials Today 15/1-2 (2012) 36.

[5] W.L. Ma, C.Y. Yang, X. Gong, K. Lee, A.J. Heeger, Advanced Functional Materials 15/10 (2005) 1617.

[6] P.G. Karagiannidis, N. Kalfagiannis, D. Georgiou, A. Laskarakis, N.A. Hastas, C. Pitsalidis, S. Logothetidis, J. Mater. Chem. 22/29 (2012) 14624.

[7] D. Minh Trung, G. Wantz, H. Bejbouji, M. Urien, O.J. Dautel, L. Vignau, L. Hirsch, Solar Energy Materials and Solar Cells 95/12 (2011) 3408.

[8] J.K. Lee, W.L. Ma, C.J. Brabec, J. Yuen, J.S. Moon, J.Y. Kim, K. Lee, G.C. Bazan, A.J. Heeger, Journal of the American Chemical Society 130/11 (2008) 3619.

[9] G. Li, V. Shrotriya, J.S. Huang, Y. Yao, T. Moriarty, K. Emery, Y. Yang, Nat. Mater. 4/11 (2005) 864.

[10] S.E. Shaheen, C.J. Brabec, N.S. Sariciftci, F. Padinger, T. Fromherz, J.C. Hummelen, Appl Phys Lett 78/6 (2001) 841.

[11] M. Westphalen, U. Kreibig, J. Rostalski, H. Luth, D. Meissner, Solar Energy Materials and Solar Cells 61/1 (2000) 97.

[12] A.J. Morfa, K.L. Rowlen, T.H. Reilly, III, M.J. Romero, J. van de lagemaat, Appl Phys Lett 92/1 (2008).

[13] J.R. Cole, N.J. Halas, Appl Phys Lett 89/15 (2006).

[14] D.H. Wang, D.Y. Kim, K.W. Choi, J.H. Seo, S.H. Im, J.H. Park, O.O. Park, A.J. Heeger, Angewandte Chemie-International Edition 50/24 (2011) 5519.

[15] X. Chen, C. Zhao, L. Rothberg, M.-K. Ng, Appl Phys Lett 93/12 (2008) 123302.

[16] G.D. Spyropoulos, M. Stylianakis, E. Stratakis, E. Kymakis, Photonics and Nanostructures-Fundamentals and Applications 9/2 (2011) 184.

[17] N. Lagos, M.M. Sigalas, E. Lidorikis, Appl Phys Lett 99/6 (2011).

[18] J.F. Zhu, M. Xue, H.J. Shen, Z. Wu, S. Kim, J.J. Ho, A. Hassani-Afshar, B.Q. Zeng, K.L. Wang, Appl Phys Lett 98/15 (2011) 151110.

[19] H.A. Atwater, A. Polman, Nat. Mater. 9/3 (2010) 205.

[20] V.E. Ferry, J.N. Munday, H.A. Atwater, Adv. Mater. 22/43 (2010) 4794.

[21] A.P. Kulkarni, K.M. Noone, K. Munechika, S.R. Guyer, D.S. Ginger, Nano Lett. 10/4 (2010) 1501.

[22] D.D.S. Fung, L. Qiao, W.C.H. Choy, C. Wang, W.E.I. Sha, F. Xie, S. He, J. Mater. Chem. 21/41 (2011) 16349.

[23] D. Qu, F. Liu, Y.D. Huang, W.L. Xie, Q. Xu, Opt. Express 19/24 (2011) 24795.

[24] J.L. Wu, F.C. Chen, Y.S. Hsiao, F.C. Chien, P.L. Chen, C.H. Kuo, M.H. Huang, C.S. Hsu, ACS Nano 5/2 (2011) 959.

[25] M. Xue, L. Li, B.J.T. de Villers, H. Shen, J. Zhu, Z. Yu, A.Z. Stieg, Q. Pei, B.J. Schwartz, K.L. Wang, Appl Phys Lett 98/25 (2011).

[26] M.A. Green, S. Pillai, Nature Photonics 6/3 (2012) 130.

[27] N. Kalfagiannis, P.G. Karagiannidis, C. Pitsalidis, N.T. Panagiotopoulos, C. Gravalidis, S. Kassavetis, P. Patsalas, S. Logothetidis, Solar Energy Materials and Solar Cells 104 (2012) 165.

[28] I. Kim, T.S. Lee, D.S. Jeong, W.S. Lee, K.-S. Lee, Journal of Physics D-Applied Physics 45/6 (2012) 065101.

[29] R.S. Kim, J. Zhu, J.H. Park, L. Li, Z. Yu, H. Shen, M. Xue, K.L. Wang, G. Park, T.J. Anderson, Q. Pei, Opt. Express 20/12 (2012) 12649.

[30] S.-W. Baek, J. Noh, C.-H. Lee, B. Kim, M.-K. Seo, J.-Y. Lee, Sci. Rep. 3 (2013) 1726.

[31] P. Drude, Zur Elektronentheorie der Metalle, Ann. Phys. (Leipzig) 566-613 (1900) 1.

[32] J.C. Maxwell Garnett, Colours in metal glasses and in metallic films rapid response, Trans. R. Soc. London 203 (1904) 385.

[33] K. Tvingstedt, N.-K. Persson, O. Inganas, A. Rahachou, I.V. Zozoulenko, Appl Phys Lett 91/11 (2007).

[34] M. Girtan, R. Mallet, D. Caillou, G.G. Rusu, M. Rusu, Superlattices and Microstructures 46/1-2 (2009) 44.

List of Figure captions

Fig. 1. Standard buffer layer (a) and a series of PEDOT:PSS layers doped with Ag NPs deposited with e-beam evaporation under different effective thicknesses: (b) 5 nm, (c) 10 nm, (d) 15 nm and (e) 20 nm.

Fig. 2. a-d) AFM images of Ag NPs on top of ITO/Glass substrate after thermal annealing process. The images a-d correspond to the different effective thicknesses of Ag (5-20 nm), e) size distribution, f) cross sectional snapshot of samples (inset depicts a magnification of the cross section of the different samples indicating a small and a large particle in sample of Fig. 2d image).

Fig. 3. a-d) AFM images of PEDOT:PSS on top of Ag NPs/ITO/Glass, e) AFM image of reference PEDOT:PSS on top of ITO/Glass substrate, f) cross sectional snapshot of samples (inset depicts a magnification of the cross section of the different samples indicating a particle in sample of Fig. 3d image).

Fig. 4. Pseudo-dielectric functions of the reference device (a) and the plasmonic ones (b-e). The legend in the graph presents the spectra of the devices in correspondence to Fig. 1.

Fig. 5. Pseudo-dielectric function (symbol and line) and fitting (solid line) of the sample with the larges particles. The fitting process was focused in the visible spectral range, where the LSPR contribution from the Ag NPs is apparent.

Fig. 6. Reflectivity measurements of s-polarized light in specular ($\theta=0^o$) and non-specular directions. The inset depicts the ratio of the total (specular + non-specular) reflectivity R over the specular reflectivity (R_s) values at an angle of inceidence of 20^o.

Fig. 7. a) The I-V characteristics of Au/PEDOT:PSS/Ag/ITO/Glass devices (b-e) in relation to the reference device (a) without Ag NPs incorporated into the PEDOT:PSS layer, b) resistivity values of the devices in relation to the average particle diameter of the Ag NPs introduced in the buffer layer.

List of Tables captions

Table 1. Table summarizing the results of the AFM analysis on the pure Ag NPs on top of the ITO/Glass substrate.

Tables (if any)

List of Tables

Ag effective thickness (nm)	Average particle size (nm)	Surface coverage (%)	Device embedded in
5	30	75	(b)
10	40	65	(c)
15	60	60	(d)
20	80	55	(e)

Fig. 1

Click here to download high resolution image

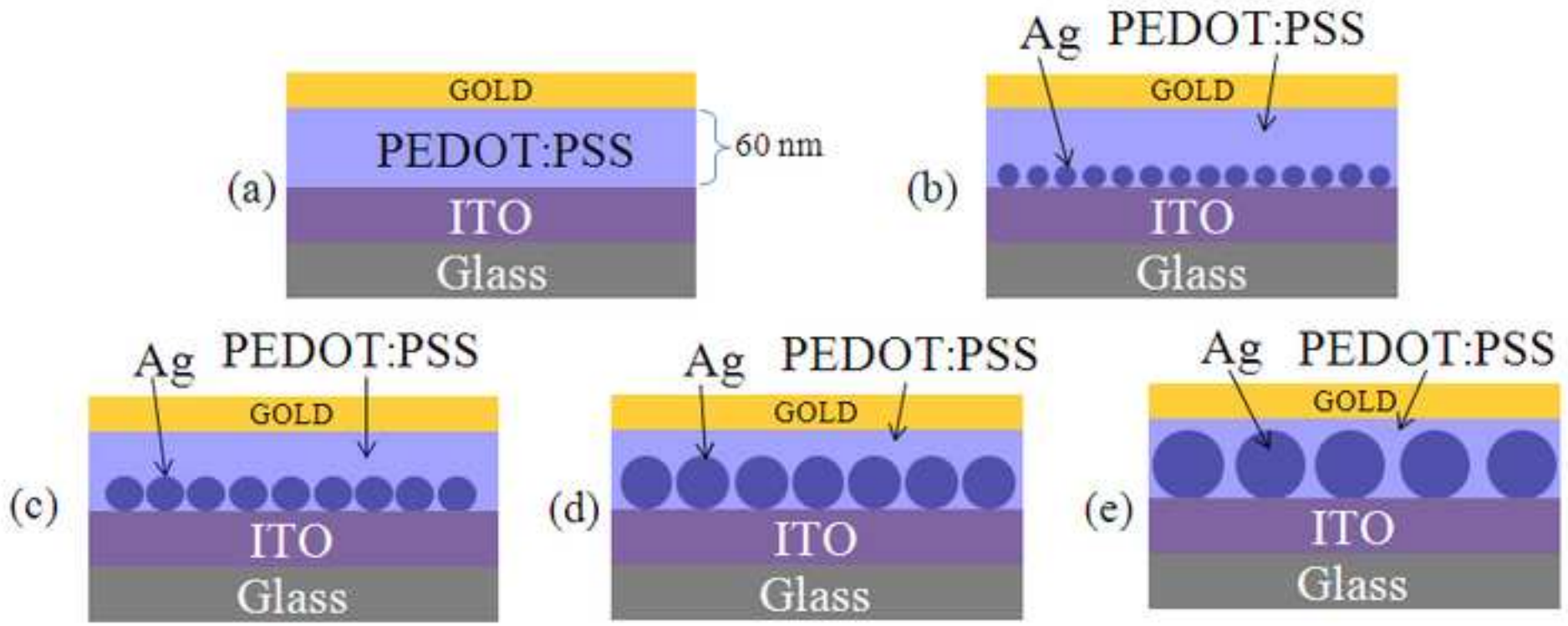

Fig. 2a

Click here to download high resolution image

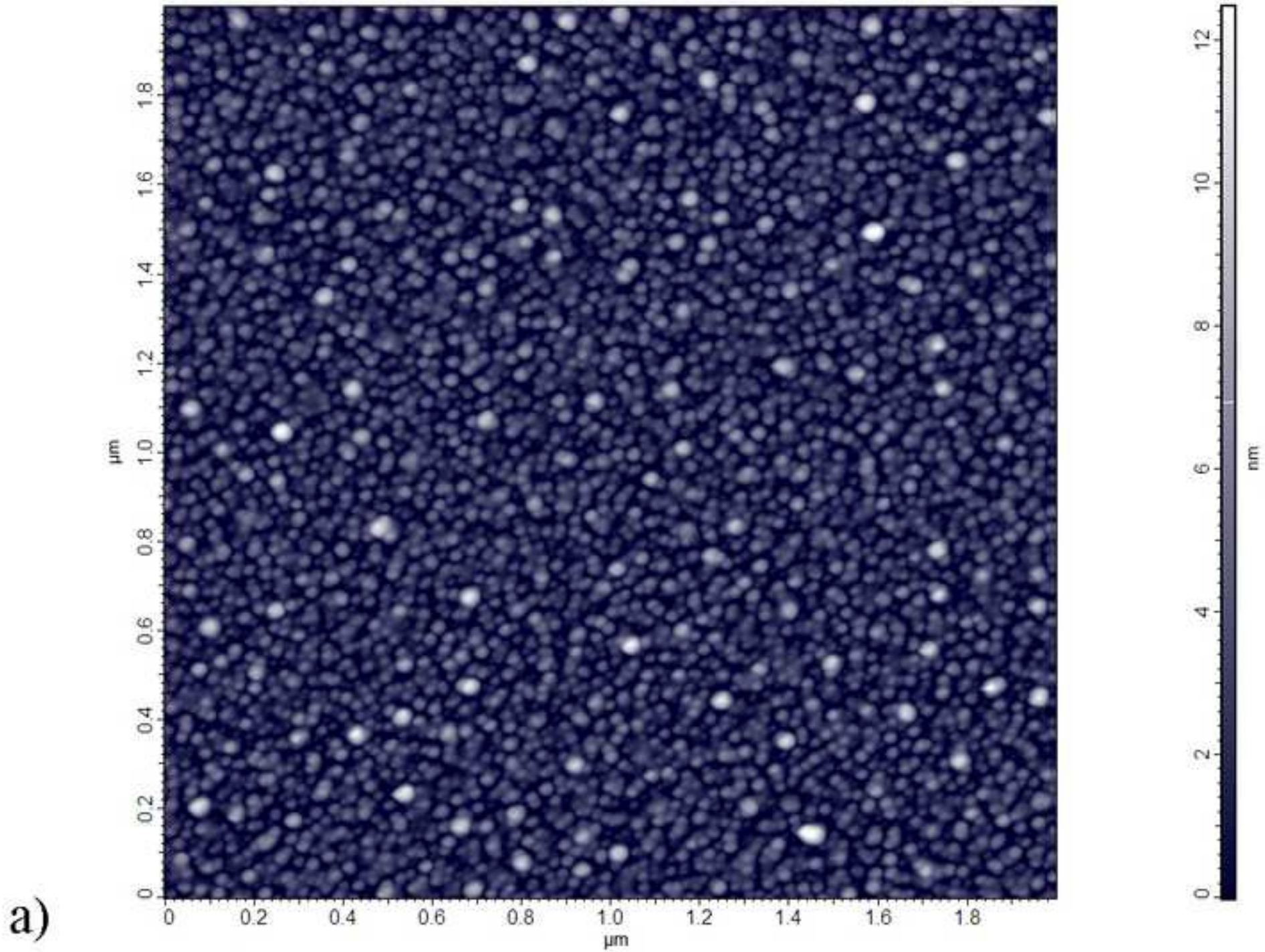

Fig. 2b

Click here to download high resolution image

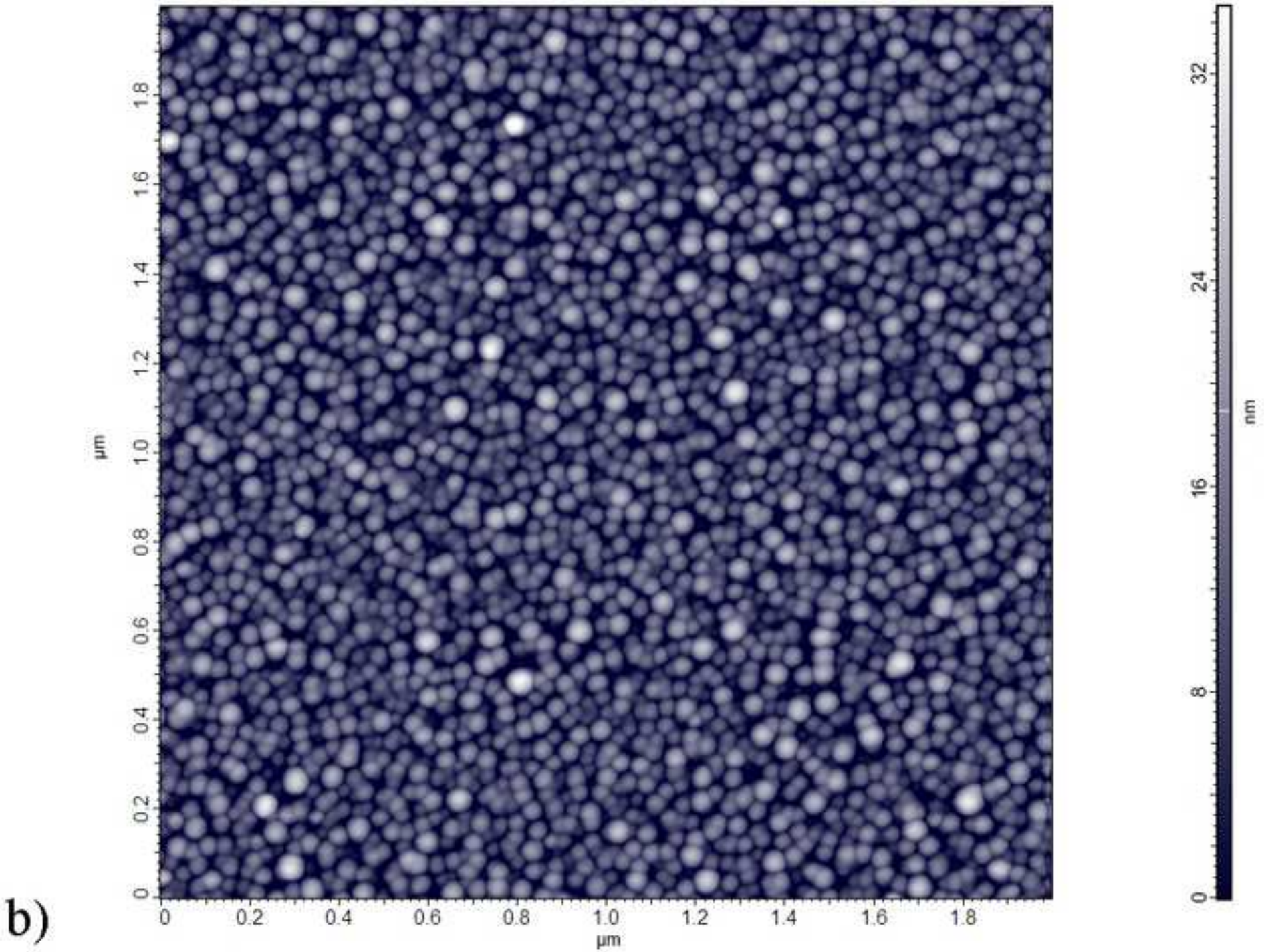

Fig. 2c

Click here to download high resolution image

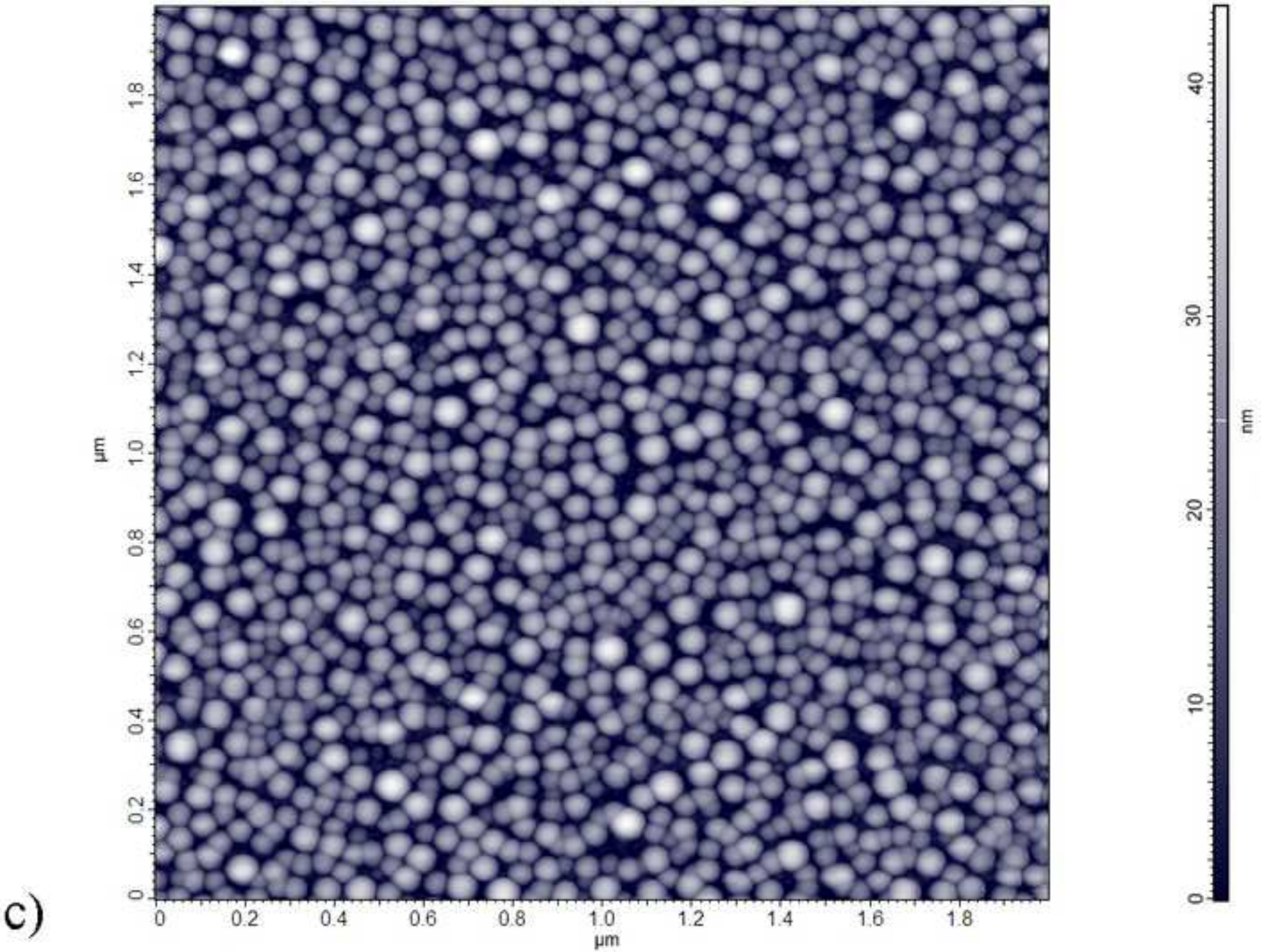

Fig. 2d

Click here to download high resolution image

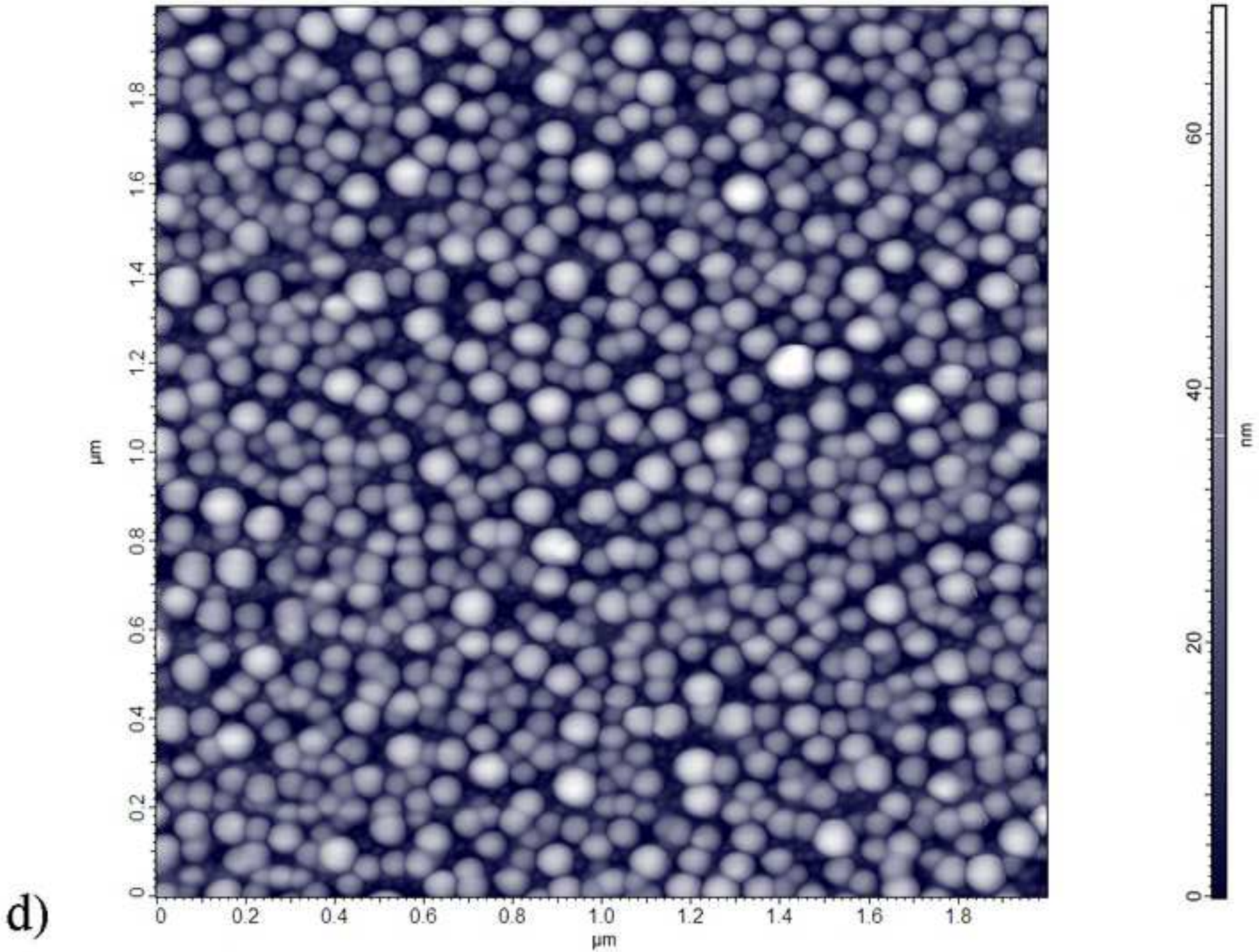

Fig. 2e

Click here to download high resolution image

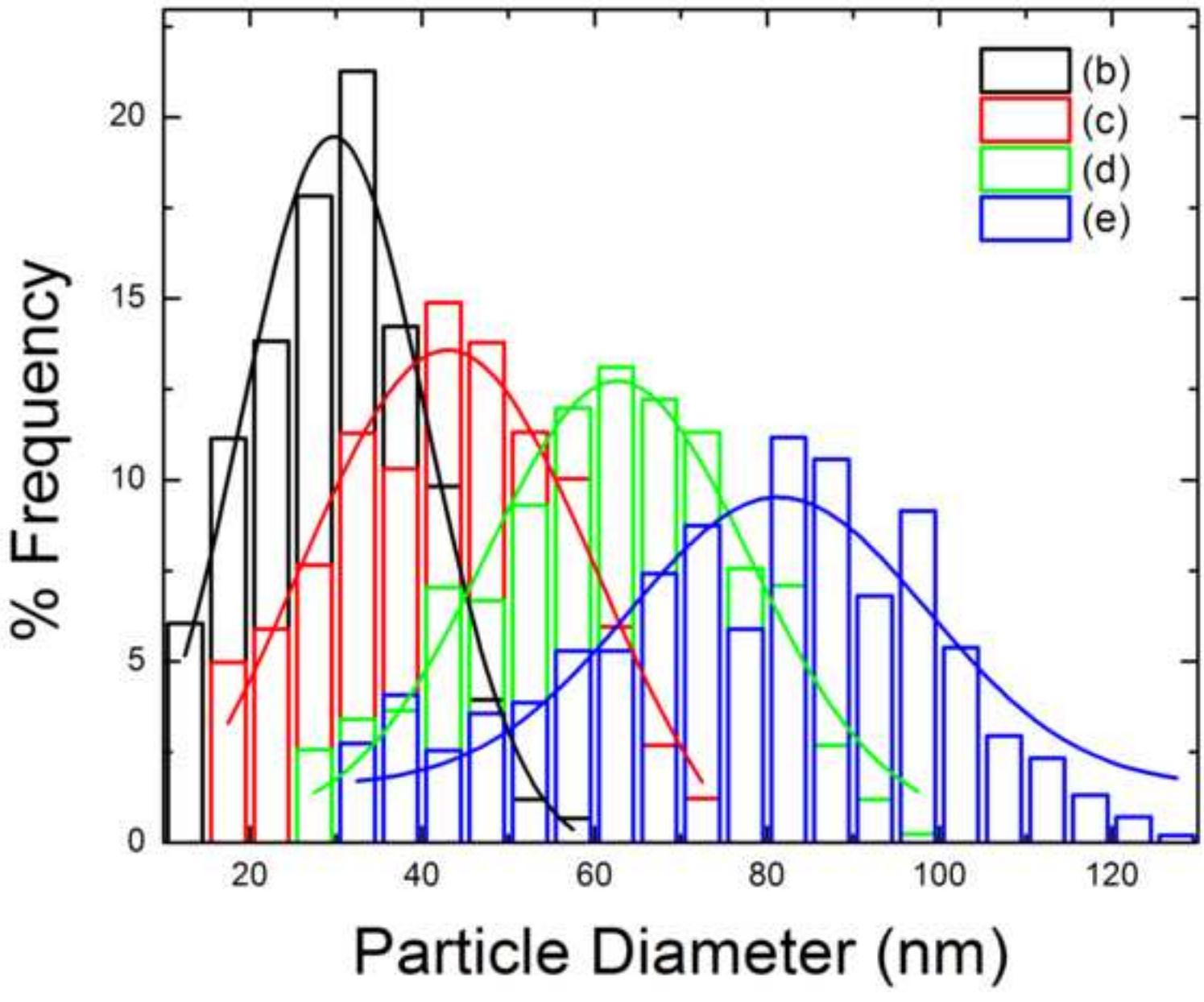

e)

Fig. 2f

Click here to download high resolution image

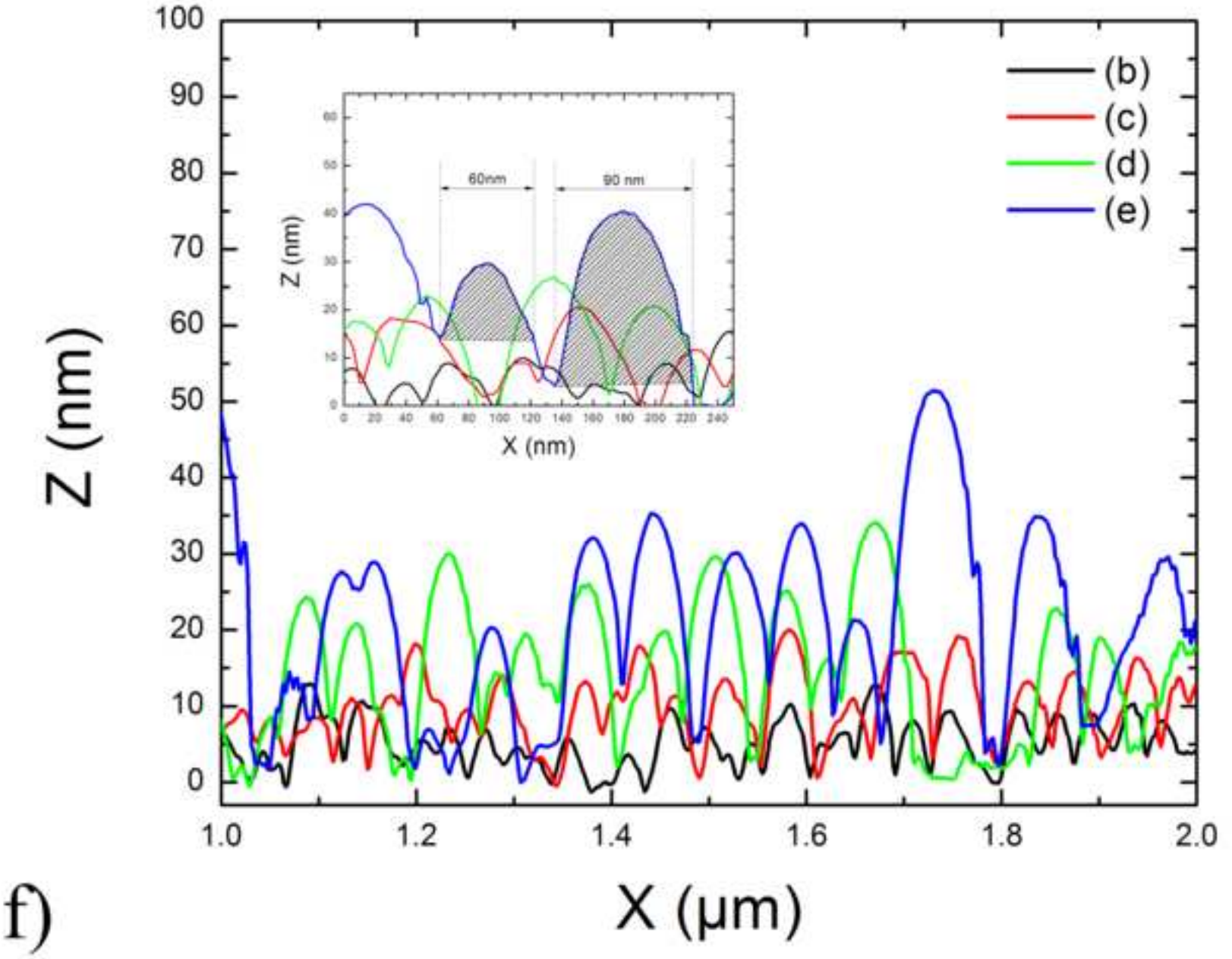

Fig. 3a

Click here to download high resolution image

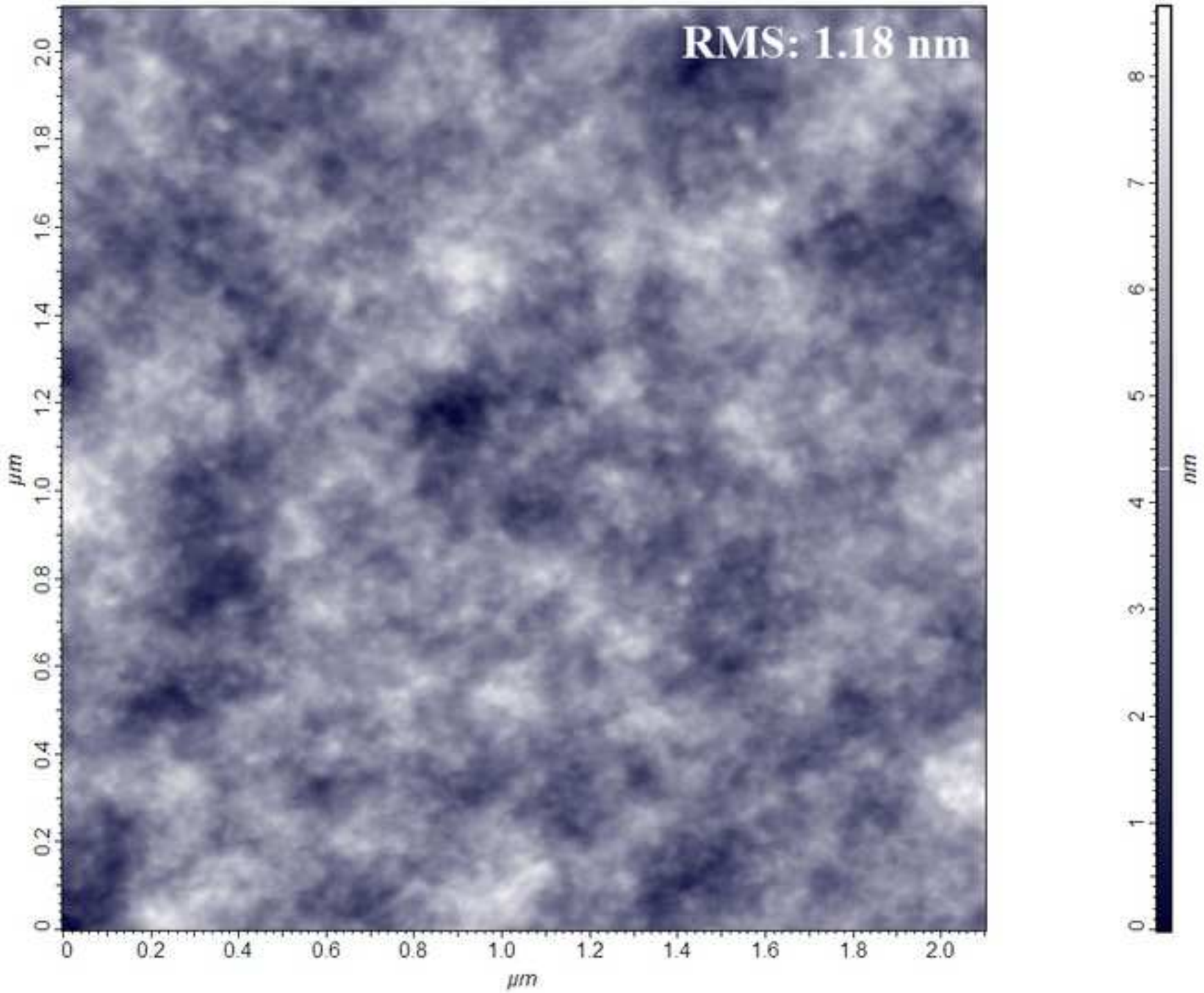

Fig. 3b

Click here to download high resolution image

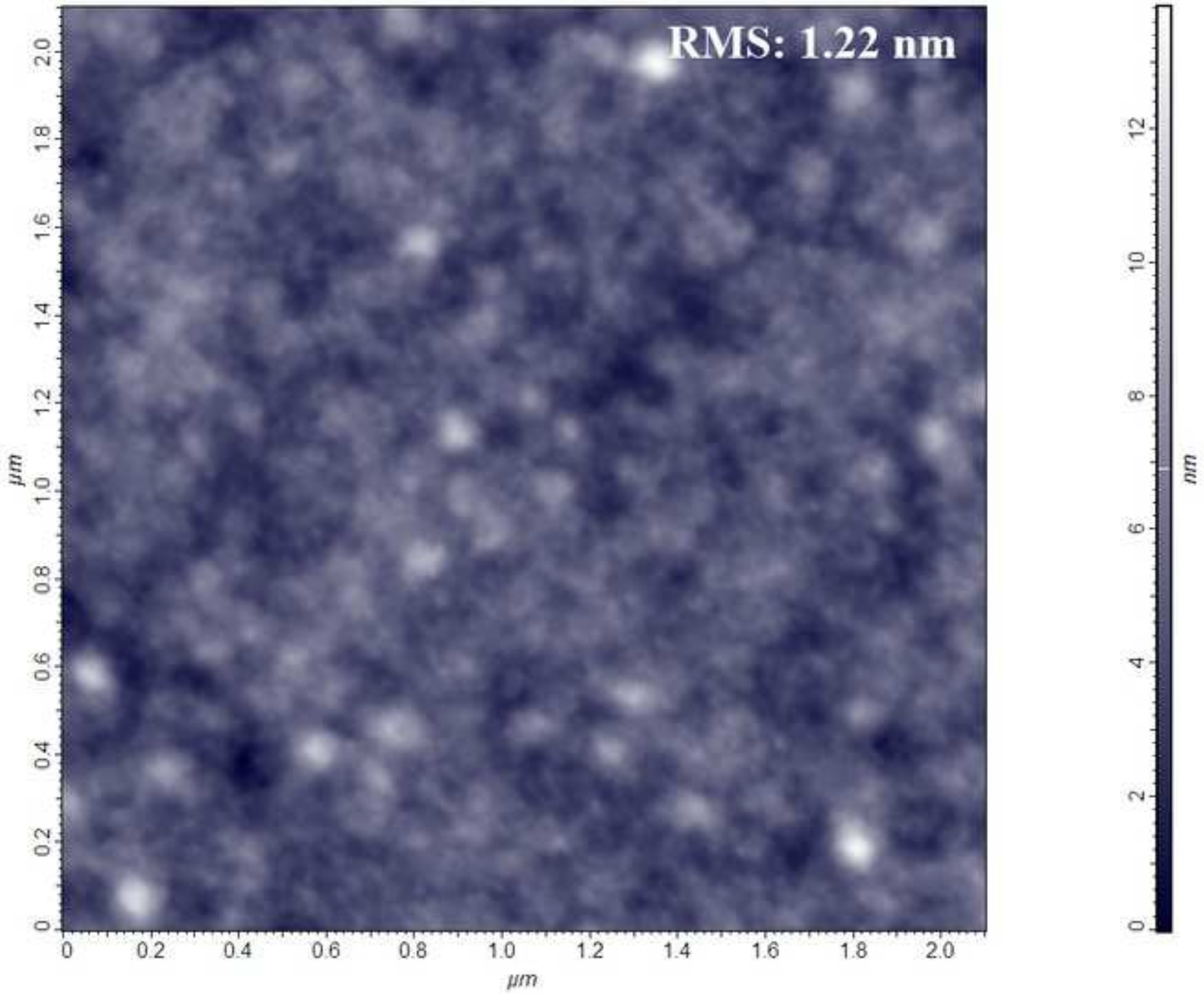

Fig. 3c

Click here to download high resolution image

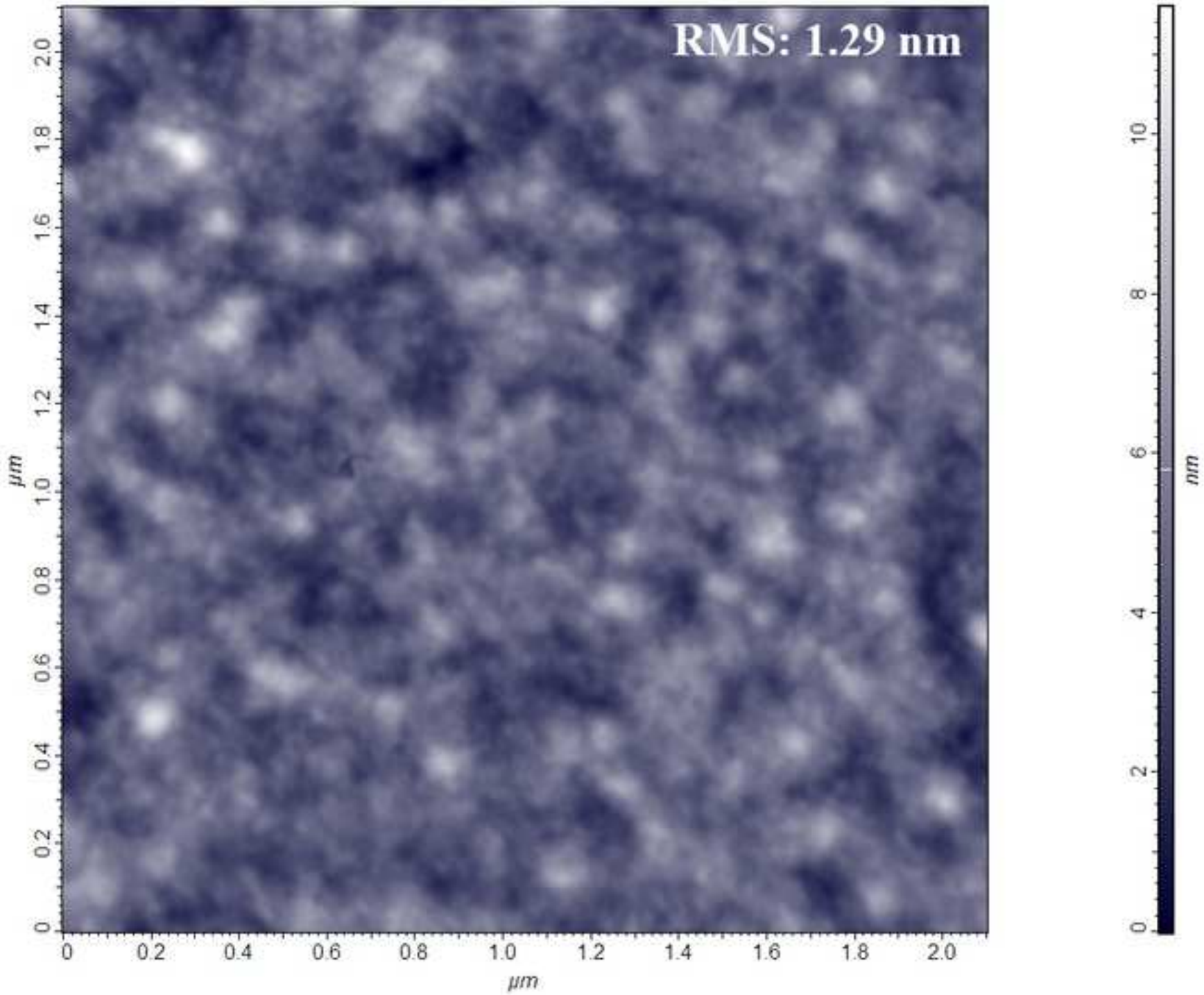

c)

Fig. 3d

Click here to download high resolution image

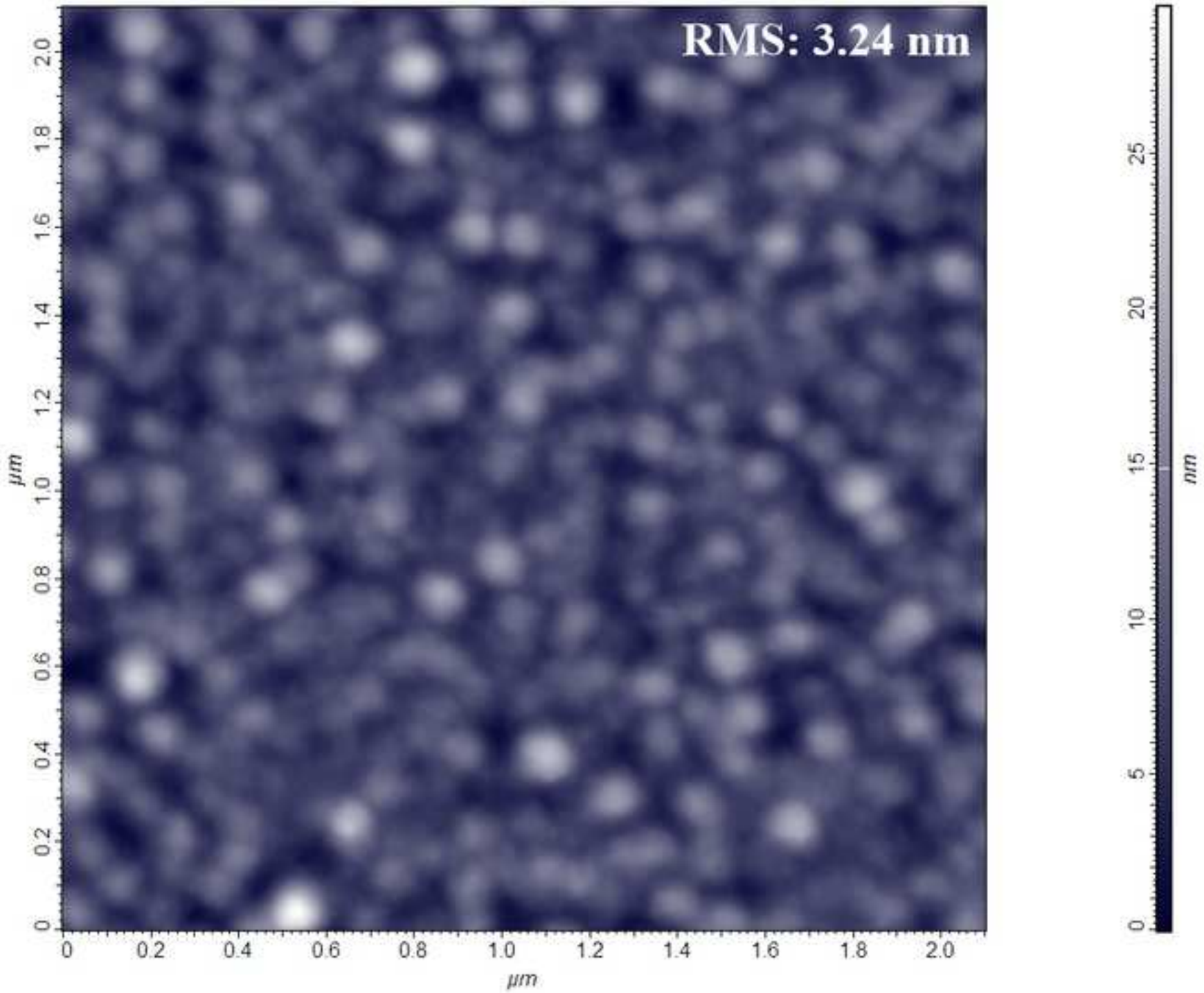

d)

Fig. 3e

Click here to download high resolution image

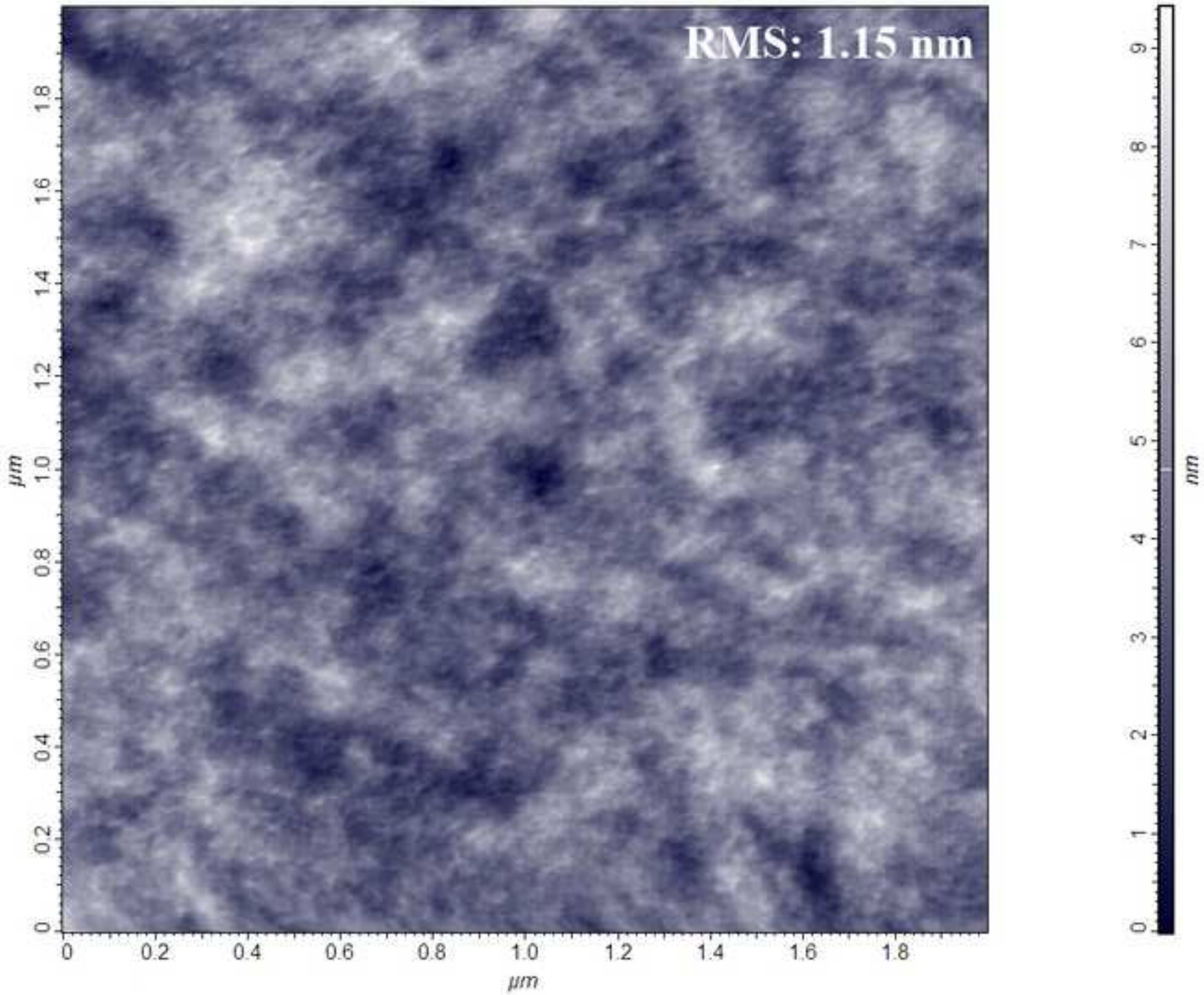

e)

Fig. 3f

Click here to download high resolution image

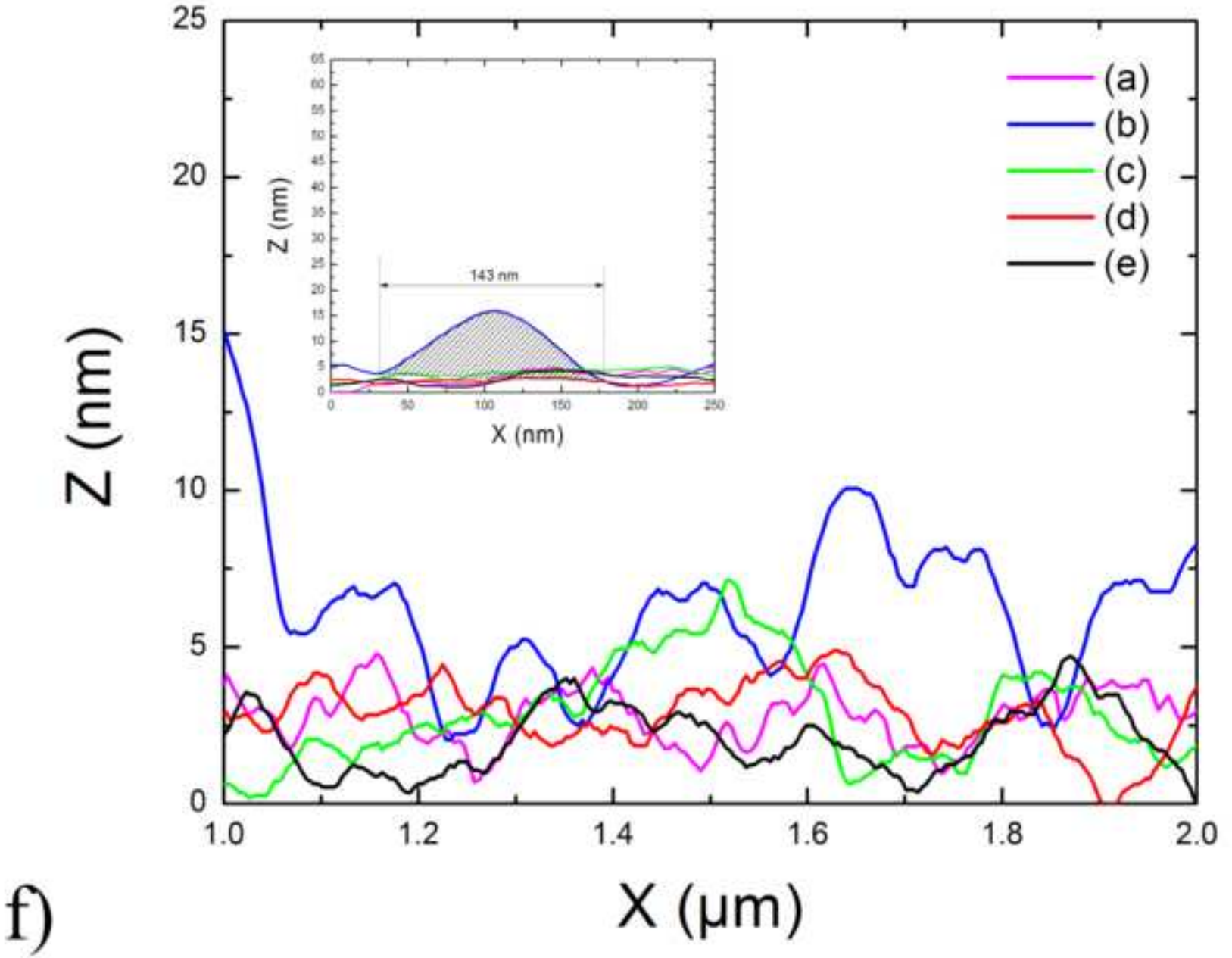

Fig. 4

Click here to download high resolution image

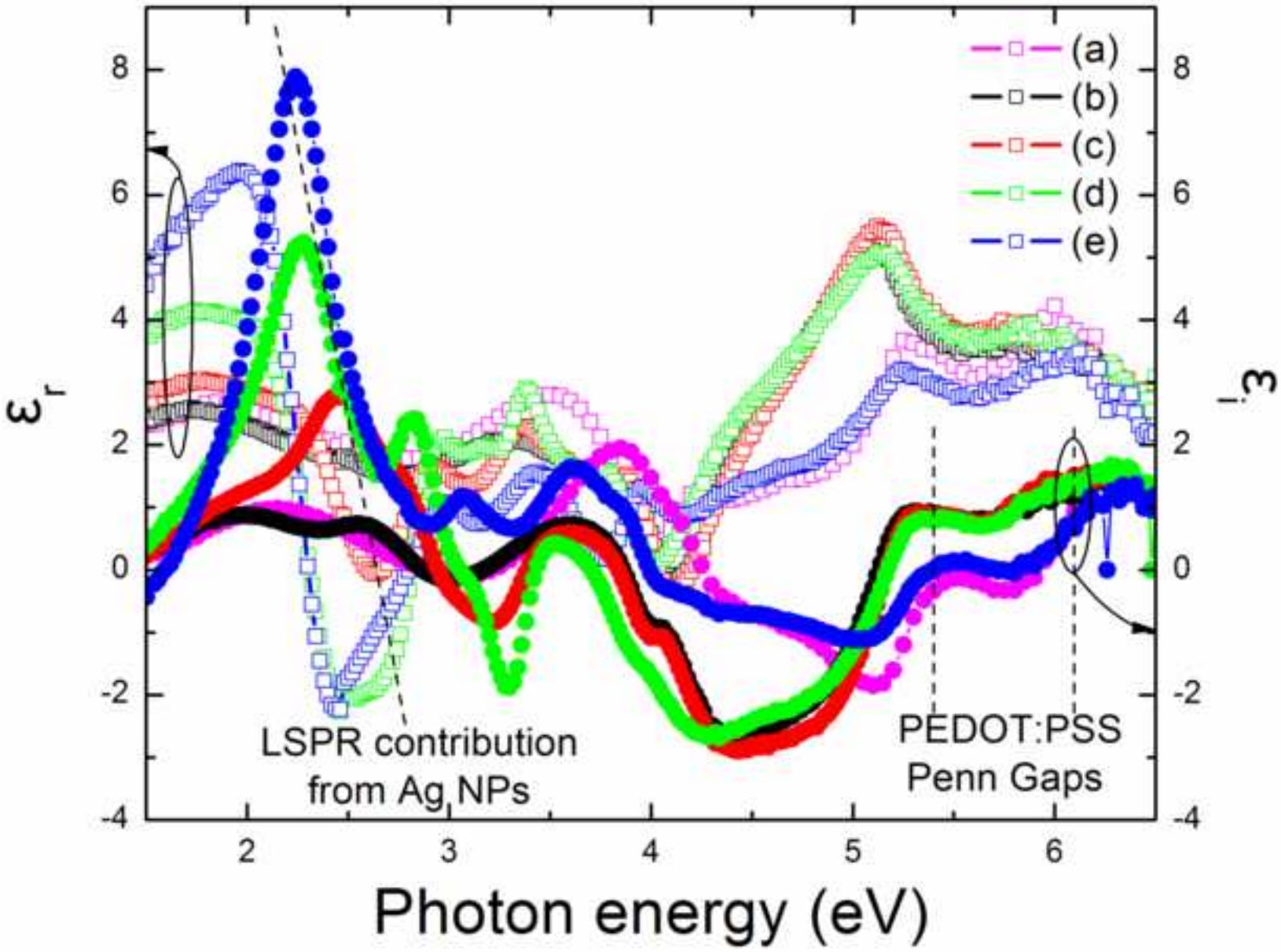

Fig. 5

Click here to download high resolution image

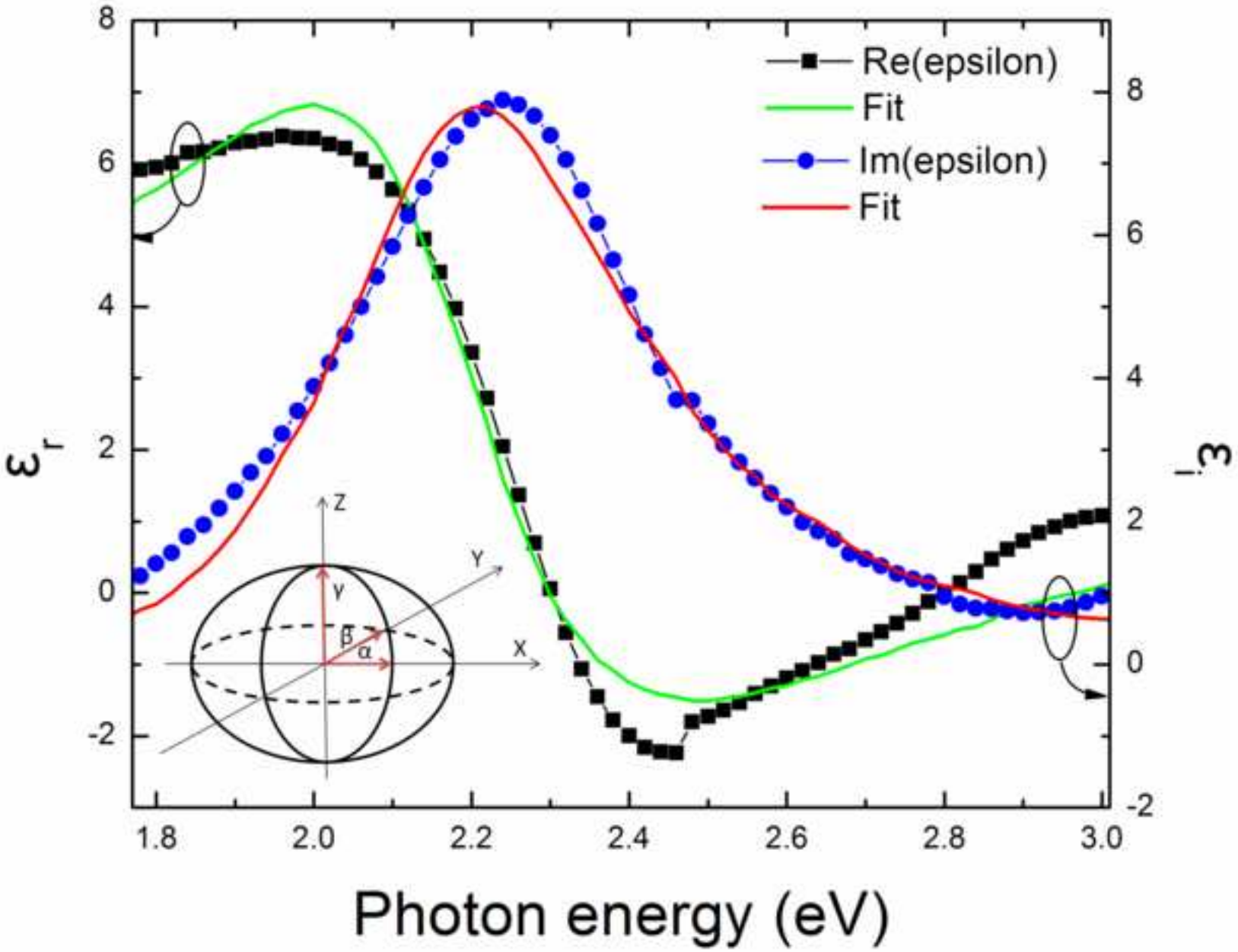

Fig. 6

Click here to download high resolution image

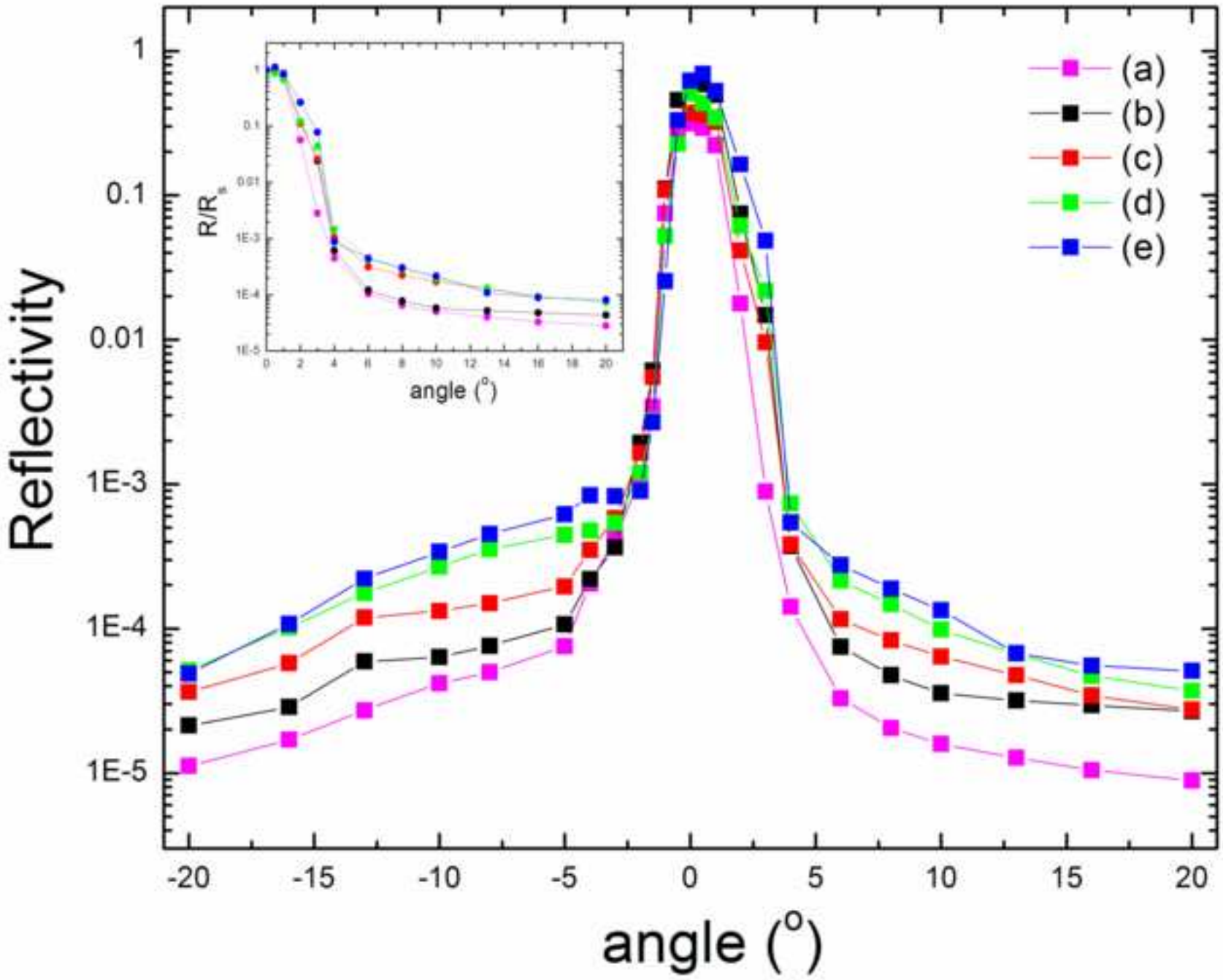

Fig. 7a

Click here to download high resolution image

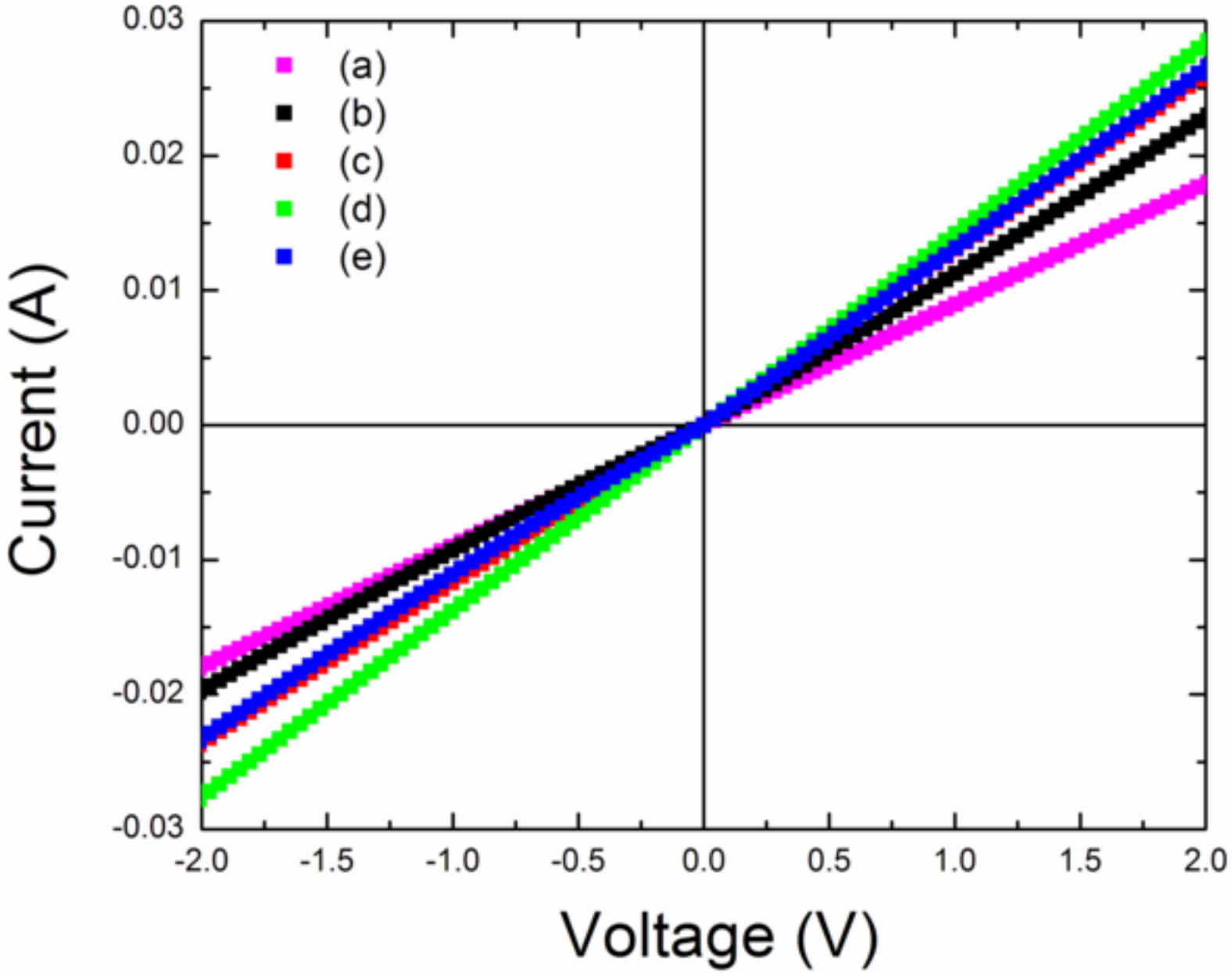

Fig. 7b

Click here to download high resolution image

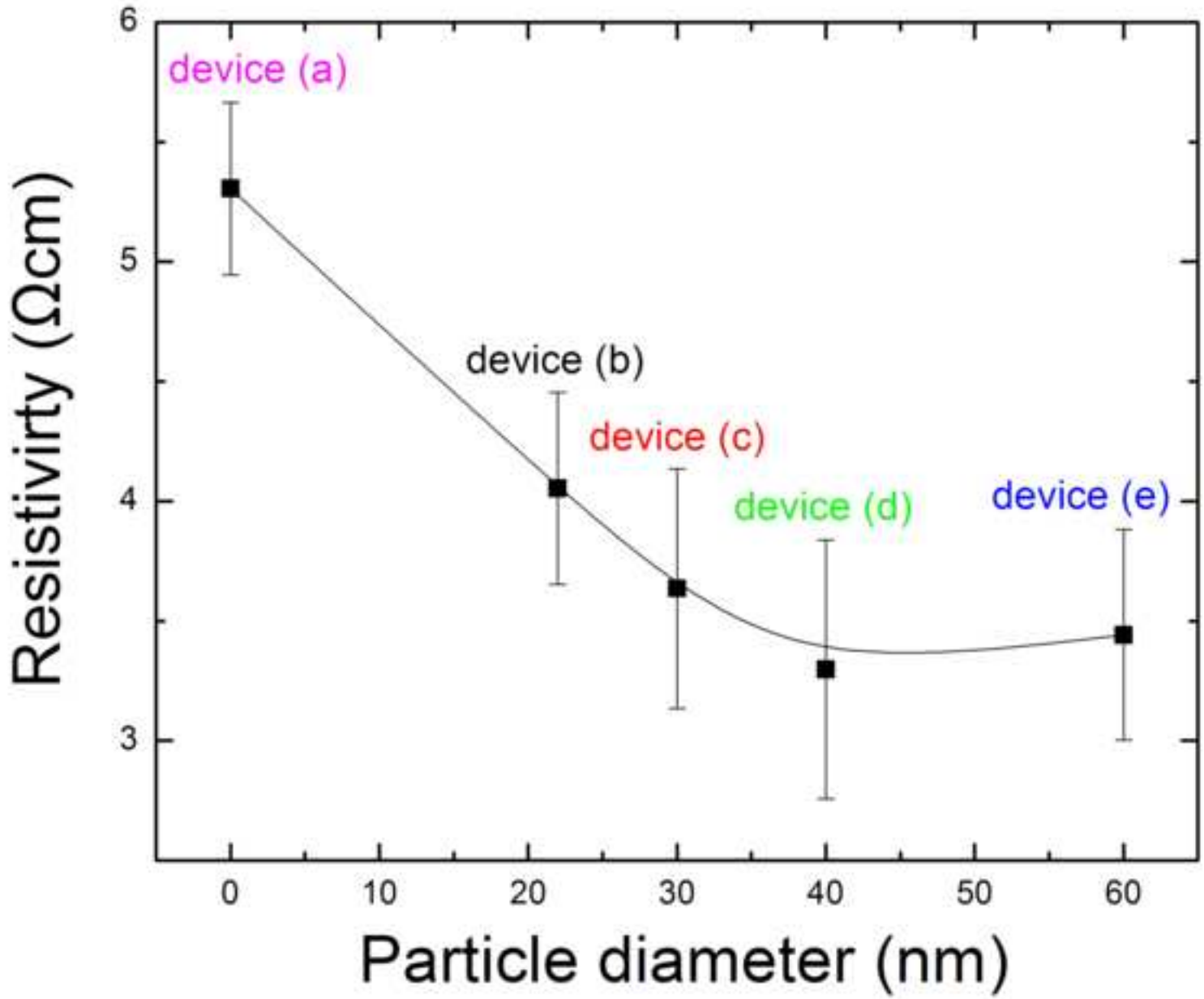

b)